

**OPEN ACCESS**

## A Novel Solid Oxide Electrochemical Oxygen Pump for Oxygen Therapy

To cite this article: Mei Wang *et al* 2022 *J. Electrochem. Soc.* **169** 064509

View the [article online](#) for updates and enhancements.

**Investigate your battery materials under defined force!**  
**The new PAT-Cell-Force, especially suitable for solid-state electrolytes!**



- Battery test cell for force adjustment and measurement, 0 to 1500 Newton (0-5.9 MPa at 18mm electrode diameter)
- Additional monitoring of gas pressure and temperature


[www.el-cell.com](http://www.el-cell.com) +49 (0) 40 79012 737 [sales@el-cell.com](mailto:sales@el-cell.com)

**EL-CELL**<sup>®</sup>  
electrochemical test equipment





# A Novel Solid Oxide Electrochemical Oxygen Pump for Oxygen Therapy

Mei Wang, Kamil Maciej Nowicki, and John Thomas SIRR Irvine<sup>\*,z</sup> 

School of Chemistry, University of St Andrews, St Andrews, Fife, KY16 9ST, United Kingdom

A solid oxide electrochemical oxygen pump was developed in tubular geometry with YSZ electrolyte and LSCF/CGO symmetrical air electrodes. The cells were manufactured based on green symmetrical porous YSZ electrode backbones cast on the green YSZ electrolyte tape, rolled into tubular geometry, co-sintered and impregnated with functional materials. The prepared cell had a thin 16  $\mu\text{m}$ -electrolyte and supporting 76  $\mu\text{m}$ -symmetric electrodes. At 700 °C, 2.8 A current (0.8 A  $\text{cm}^{-2}$ ) was obtained under 0.5 V in the single tubular cell infiltrated with 30% CGO and 45% LSCF. A four cell bundle produced theoretical 1.82 l  $\text{hr}^{-1}$  O<sub>2</sub> with a power consumption of 2.18 W at 700 °C. Excellent stability of the cells was achieved during severe current and thermal cycling tests, indicating the successful fabrication of the tubular cells using the tape co-casting method.

© 2022 The Author(s). Published on behalf of The Electrochemical Society by IOP Publishing Limited. This is an open access article distributed under the terms of the Creative Commons Attribution 4.0 License (CC BY, <http://creativecommons.org/licenses/by/4.0/>), which permits unrestricted reuse of the work in any medium, provided the original work is properly cited. [DOI: 10.1149/1945-7111/ac7008]



Manuscript submitted February 4, 2022; revised manuscript received April 8, 2022. Published June 15, 2022. *This paper is part of the JES Focus Issue on Focus Issue In Honor of John Goodenough: A Centenarian Milestone.*

Supplementary material for this article is available [online](#)

High-purity oxygen is an essential industrial gas to manufacture products in processes involving combustion or chemical reaction with oxygen. When utilised for medical purposes, oxygen is used in respiratory disease treatments, requiring a high purity of 99% in the United States and 99.5% in Europe. The experience acquired during the COVID peaks showed that the limited ventilators and space in hospitals could not meet the enormous demand for oxygen, imposing a need for small scale and portable oxygen treatment systems out with the hospital and intensive care units.

Three main technologies have been used for oxygen production: cryogenic distillation, pressure swing adsorption (PSA) and membrane separation<sup>1</sup>. Cryogenic distillation is technologically mature and most commonly used for oxygen production on an industrial scale (100–300 tons/day),<sup>2–5</sup> with O<sub>2</sub> purity up to 99%. However, logistical problems, such as a requirement for frequent replacement and safety hazards associated with the handling of pressurised containers, make the cryogenic distillation impractical for many applications. PSA<sup>6–8</sup> is a typical approach for producing O<sub>2</sub> (>95% purity) at a medium scale plant (20–100 tons/day), involving a repeated adsorption/desorption process by using packed columns with adsorbents, such as zeolites and activated carbons.<sup>9</sup> The product purity and production scale can be manipulated by the number of beds in series.<sup>5</sup> Both cryogenic distillation and PSA are considered as too energy intensive, while membrane separation has been attractive for O<sub>2</sub> production in smaller scale scenarios (10–25 tons day<sup>-1</sup>) and medium purity (25%–40%) at manageable cost.<sup>5</sup> However, there is a “tradeoff” in performance between its permeability and selectivity while using the polymeric membranes. Developing membrane materials with both higher permeability and selectivity is thus a critical issue to improve the O<sub>2</sub> purity and to make the membrane separation technique more competitive and energy efficient.<sup>5</sup>

The new membranes based on ceramic or perovskite materials can selectively transport oxygen in the form of an ionic flux at high temperatures, producing O<sub>2</sub> of extremely high purity.<sup>10</sup> The ceramic membrane can either be a pure oxygen-ion conductor driven functioned by a potential difference (e.g., Y<sub>2</sub>O<sub>3</sub> or Sc<sub>2</sub>O<sub>3</sub> doped zirconia, doped CeO<sub>2</sub>, LaGaO<sub>3</sub>, doped Bi<sub>2</sub>O<sub>3</sub> and BiMVO<sub>x</sub>) or mixed electron and oxygen-ion conductor driven by the differential O<sub>2</sub> partial pressure across the membrane (e.g., doped SrCoO<sub>3- $\delta$</sub> , La<sub>1-x</sub>Sr<sub>x</sub>Ga<sub>1-y</sub>FeyO<sub>3+ $\delta$</sub> , La<sub>1-x</sub>Sr<sub>x</sub>Ga<sub>1-y</sub>CoyO<sub>3+ $\delta$</sub> ,

Sr<sub>4</sub>Fe<sub>6-x</sub>Co<sub>x</sub>O<sub>13+ $\delta$</sub> ).<sup>10–16</sup> Apart from the zirconia-based materials, most of these materials have low chemical stability, poor mechanical properties, or difficulty in fabrication of suitable structures. For the electric voltage driven membrane separation, it is in fact an oxygen electrolysis process from ambient air based on solid oxide cells,<sup>17–19</sup> where the oxygen is electrochemically pumped<sup>20</sup> through the dense oxygen ion-conducting membrane. Thus a device is thus called an oxygen pump (oxygen pump). In the process, oxygen from the air is electrolysed to ions at a cathode, transferring through the oxygen ion-conducting electrolyte and liberated as pure oxygen gas at an anode. The oxygen pump provides high oxygen purity because only oxygen ions can diffuse through the electrolyte membrane.<sup>21</sup> Unlike the solid oxide fuel cells or solid oxide electrolysis cells, the oxidised environments on both the anode and cathode sides in oxygen pump allows the use of the same materials on both electrodes, which is much easier to implement.

Compared with planar geometry, a tubular design of the oxygen pump cell is preferable. It provides a natural separated space of air and oxygen gas and simplifies the heat distribution evolved in the course of operation.<sup>20,22</sup> Also, the tubular cells have good mechanical strength and stability during thermal cycling and are easily scalable.<sup>23–26</sup> An oxygen pump based on tube solid oxide cells was studied by Spirin, et al.,<sup>20</sup> with YSZ supporting electrolyte (150  $\mu\text{m}$ ) and symmetrical LSM electrodes (20  $\mu\text{m}$ ). The specific power consumption was 1 kWh m<sup>-3</sup> in a single tubular cell at the temperature of 780 °C and a current density of 0.3 A  $\text{cm}^{-2}$ . The bundle of three tubular cells connected in series produced 9 l  $\text{hr}^{-1}$  of pure oxygen at 800 °C at a power consumption of 50 W.

La<sub>0.6</sub>Sr<sub>0.4</sub>Co<sub>0.2</sub>Fe<sub>0.8</sub>O<sub>3- $\delta$</sub>  (LSCF) is the most investigated mixed ionic and electronic (MIEC) perovskite oxygen electrode, having high catalytic activity towards oxygen reduction at intermediate temperature range (600 °C–800 °C).<sup>27–30</sup> However, highly resistive layer of SrZrO<sub>3</sub> and La<sub>2</sub>Zr<sub>2</sub>O<sub>7</sub> can form due to the reaction between LSCF and YSZ during cell manufacturing at a temperature above 1000 °C deteriorating the cell performance.<sup>21,31,32</sup> A thin dense doped ceria layer, such as gadolinium-doped ceria (CGO), is often applied between the YSZ electrolyte and LSCF electrode to minimise the reactivity during cell manufacturing and electrochemical test,<sup>33–36</sup> although the insulating SrZrO<sub>3</sub> phase still can be detected after a long-term test.<sup>37</sup> Impregnation (infiltration) has been found to be an effective way to introduce nanostructured electrode materials onto the electrolyte scaffold at a lower temperature, not only minimising the reactivity during manufacturing between the cell components,<sup>38–40</sup> but also alleviating the problems caused by thermal incompatibility between components. Furthermore, the

\*Electrochemical Society Fellow.

<sup>z</sup>E-mail: [jtsi@st-andrews.ac.uk](mailto:jtsi@st-andrews.ac.uk)

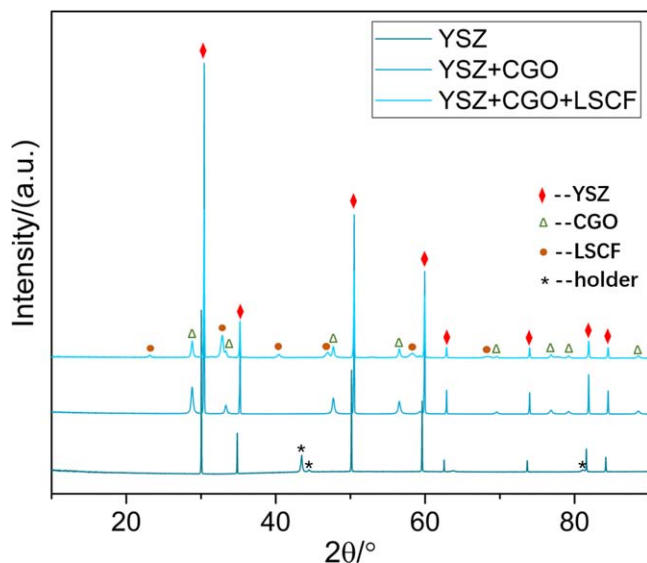


**Figure 1.** X-ray diffraction patterns for YSZ, YSZ scaffold impregnated with CGO, and further impregnated with LSCF.

nanoparticles introduced by impregnation enlarge the triple-phase boundary for electrochemical reactions, significantly enhancing the cell performance.

This work presents the fabrication of the tubular cell from a tape co-casting method that is flexible to scale up in cell size and number. A sequential casting technique was used where all the functional layers in cells assembly were cast on each other, giving a strong interface between layers. The co-sintered cell's scaffold comprises a thin YSZ electrolyte (16  $\mu\text{m}$ ) and symmetrical YSZ scaffold (75  $\mu\text{m}$ ). For the first time, the CGO barrier layer is introduced to the YSZ porous scaffold by an impregnation method, in order to prevent the interaction between the YSZ scaffold and following impregnated LSCF functional materials. An electrochemical oxygen generator was built combining four tubular cell into a bundle, and the electrochemical performance and oxygen generation rate were measured.

## Experimental

**Cell manufacturing.**—Cell skeleton assembly: the tape casting technique was used to produce the YSZ electrolyte and the symmetric porous YSZ scaffold. The process used for tape casting is based on that given previously.<sup>41</sup> The compositions of electrode materials were optimised on the planar cell and then implemented into the tubular cell design. The fabrication of the planar cell skeleton was achieved by laminating three single layers, with 1.16  $\text{cm}^2$  of electrode area, and normalised to 1  $\text{cm}^2$  in the electrochemical results. While for the tubular cell assembly, the tape casting technique was adopted by casting the electrode tape firstly on the polymer carrier film (Mylar) followed by casting a thin layer of electrolyte on top of the green electrode tape after it dried overnight. The same procedure was conducted to cast the other electrode layer on top of the electrolyte. The co-cast assembly was rolled into a tubular geometry with an electrode surface area of 3.5  $\text{cm}^2$ . After assembly, the cell was calcined at 1000  $^\circ\text{C}$  for 5 h to burn off the organics and fired at 1450  $^\circ\text{C}$  for 5 h to form porous scaffold and dense electrolyte layers.

**Impregnation of electrodes:** electrochemically active electrode materials were applied to the YSZ scaffold by the impregnation method. Impregnation solutions of LSCF and CGO were prepared by dissolving the nitrates of the precursors in ethanol and deionised water (1:1 in volume) according to the stoichiometry. The high purity precursors are  $\text{La}(\text{NO}_3)_3 \cdot 6\text{H}_2\text{O}$  (Alfa Aesar, 99.9%),  $\text{Sr}(\text{NO}_3)_2$  (Merck, 99.0%),  $\text{Co}(\text{NO}_3)_2 \cdot 6\text{H}_2\text{O}$  (Acros organics, 99.0%) and

$\text{Fe}(\text{NO}_3)_3 \cdot 9\text{H}_2\text{O}$  (Merck, 98.0%) for LSCF solution, and they are  $\text{CeO}_2$  (Alorich, 99.0%) and  $\text{Gd}_2\text{O}_3$  (Alfa Aesar, 99.9%) for CGO solution. Citric acid (Acros organics, 99.5%) was also added to the LSCF solution to promote phase formation.<sup>42</sup> The precursor solution was introduced drop-wise onto the porous YSZ electrode support using a 10  $\mu\text{l}$  capacity of the micropipette, dried in an oven at 80  $^\circ\text{C}$  for 30 min and calcined at 850  $^\circ\text{C}$  for 3 h. This process was repeated 4–7 times until achieving the desired loading.

**Electrochemical test and oxygen generators from air.**—Silver paste was painted on both electrode sides as a current collector. The planar cell was sealed with a ceramic sealant (Aremco Ceramabond<sup>TM</sup>) in a homemade testing jig, and the tubular cell was mounted on a stainless-steel tube.

Electrochemical tests were carried out with a Solartron 1255 Frequency Response Analyser, Solartron 1287 Electrochemical Interface, CorrWare v3.2c and Zplot v3.2c software (Scribner Associates). Electrochemical impedance spectroscopy (EIS), current-voltage (I–V) curve, potentiostatic and galvanostatic tests were used to characterise the cells' electrochemical performance in the temperature range 650  $^\circ\text{C}$ –800  $^\circ\text{C}$  with 50  $^\circ\text{C}$  intervals. The impedance spectra were collected with an amplitude of 20 mV over a frequency range of 0.2 Hz to 50 kHz. The series resistance  $R_s$  and polarisation resistance  $R_p$  are extracted from the impedance spectrum. Specifically,  $R_s$  derives from the ohmic losses of the electrolyte and the electrode materials, the contact resistance at the electrode/electrolyte interface, electrical wires and the equipment. while  $R_p$  derives from electrode processes related to the charge transfer at the electrode/electrolyte interface at high frequency, the combination of electrode reaction and charge diffusion processes at medium frequency, and the mass transfer process at the electrode surface at low frequency.<sup>43–45</sup> ASR is the area-specific resistance, a sum of the series resistance and the polarisation resistance. The  $R_s$  value was extracted from the intercept at high frequencies, and the  $R_p$  was obtained from a distance between the intersect at high frequency and low frequency, divided by 2 for one electrode.

During the test, ambient air with a flow rate of 175  $\text{ml min}^{-1}$  and 700  $\text{ml min}^{-1}$  were supplied to the single tubular cell and the four-cells bundle, respectively. A spiral geometry of the inlet gas tube was applied to warm up the air without cooling the system under the high air flow rate. The generated oxygen flow rate was measured by using a graduated flask filled with lather, and the calculation of its theoretical value is illustrated in the supporting information. The outlet of the tubular cell was connected with a mass spectrometry instrument (MKS Cirrus Mass Spectrometer) to analyse the gas composition in the anode.

The oxygen pump stays at the standby mode at a relatively low temperature when oxygen is not being used in practical operation. However, when oxygen is needed to supply to the patients, a rapid start-up of the oxygen pump is required. Therefore, good thermal cycling stability is essential for long and efficient operation. The single tubular cell's resistance to rapid temperature changes was investigated by inserting the cell directly into a furnace at 700  $^\circ\text{C}$  and taking it out directly to room temperature. The recorded temperature indicated that it takes about 2 min for the cell to reach 700  $^\circ\text{C}$  when inserting it or 100  $^\circ\text{C}$  when taking out. The cell was thermally cycled between room temperature and 700  $^\circ\text{C}$  for 18 times. The current was recorded during the cycling test under the potentiostatic mode at 0.5 V.

**Phase identification.**—The crystalline phases of the YSZ scaffold and impregnated electrode materials were analysed by X-ray diffraction (XRD). The room temperature XRD (RT-XRD) patterns were collected on a PANalytical X-ray diffractometer in a  $2\theta$  range of 10 $^\circ$ –90 $^\circ$  operating with  $\text{CuK}\alpha$  radiation ( $\lambda = 1.5406 \text{ \AA}$ ).

**Microstructure analysis.**—The electrolyte and electrodes' microstructure was investigated by Scanning Electron Microscopy (SEM) on an FEI Scios DualBeam microscope, equipped with a

secondary electron, backscattered electron detectors and an antic EDS analysis system. High-resolution observation of the interface between the YSZ scaffold and the coated CGO and LSCF layer was realised by Transmission Electron Microscopy (TEM) characterisation, while the cross-sectioned sample was prepared by focused ion beam SEM (FIB-SEM) technique.

## Results and Discussion

**Optimisation on planar cells.**—Phase identification was accomplished by XRD. Figure 1 shows the XRD patterns of the sintered YSZ tape and the impregnated cell. A pure YSZ phase is present with a cubic crystal structure, and additional peaks after impregnation correspond to CGO and LSCF, respectively. No impurity phases from their chemical reaction with the YSZ scaffold are observed.

Before developing the tubular cell approach, the effect of CGO and LSCF concentration on the cell's performance was studied in the planar configuration. As shown in Fig. S1 (available online at [stacks.iop.org/JES/169/064509/mmedia](https://stacks.iop.org/JES/169/064509/mmedia)), the thickness of the electrolyte and the symmetric electrode of the planar cell are 130  $\mu\text{m}$  and 100  $\mu\text{m}$ , respectively. Ideally, the impregnated CGO would form a dense, continuous coating on the YSZ scaffold to prevent the reaction between LSCF and YSZ. The amount of impregnated CGO was adjusted between 0% to 60 Vol% to find the optimal concentration for stabilising the LSCF (i.e. in range 26 to 40 Vol%) materials. As shown in Fig. 2, after the potentiostatic test at 0.5 V for 20 h, the performance loss mainly comes from the increase of ohmic resistance ( $R_s$ ). Comparing the current degradation rate of the cells after the 20 h operation, it decreases with a higher amount of CGO. The cell with 60% CGO + 26% LSCF has the lowest degradation rate of only 0.05%  $\text{h}^{-1}$ . Although the cell without CGO coating shows a smaller initial impedance due to the better LSCF percolation for higher electric conductivity,<sup>46</sup> it degrades quite quickly, with a degradation rate of 1.49%  $\text{h}^{-1}$ . Increasing LSCF concentration to

40% did not change the degradation rate much compared with 26% LSCF. The significant increase of  $R_s$  in the cell without the CGO barrier indicates that the CGO layer has effectively minimised the reactivity between LSCF and YSZ.

In evaluating the cell's performance, impedance and I-V data should be taken into consideration as well as the stability. As shown in Fig. S2, that  $R_s$  remains stable when coating CGO between 30% and 50%, at a value of 1.38  $\Omega\text{cm}^2$ , and it increases to 1.48  $\Omega\text{cm}^2$  with 60% CGO. Meanwhile, the  $R_p$  decreases slowly in the whole CGO concentration range of 30%–60%. The ASR value is comparable in the CGO concentration range of 30%–50% but slightly higher in 60% CGO. With a higher LSCF impregnation amount of 40%, the  $R_s$  (1.00  $\Omega\text{cm}^2$ ) and  $R_p$  (0.10  $\Omega\text{cm}^2$ ) are much smaller than that with 26% LSCF (1.38  $\Omega\text{cm}^2$  and 0.18  $\Omega\text{cm}^2$  for  $R_s$  and  $R_p$  respectively) because LSCF phase percolates a random structure much better.<sup>39</sup> While the current density at 0.5 V of the cell impregnated with 26% LSCF is only 0.36  $\text{A cm}^{-2}$  regardless of the CGO amount, the cell with 40% LSCF has a current density at 0.5 V of 0.53  $\text{A cm}^{-2}$  (Fig. 3b). Summarising, based on the results from the cell stability and IV performance test, the optimum performance was attained for the impregnation amount of 50% CGO and 40% LSCF.

**Single tubular oxygen pump cell performance.**—For the single tubular oxygen pump cell in this section, its skeleton was assembled by laminating one single porous YSZ layer with the co-cast layer (porous YSZ + dense YSZ). 50% CGO and 40% LSCF were supposed to be impregnated to the tubular scaffold; however, after infiltrating 50% CGO and 35% LSCF, the outer electrode seemed to be saturated and difficult to adsorb more solution. Herein, the tubular cell had a slightly lower LSCF concentration than in the electrode optimised in planar configuration.

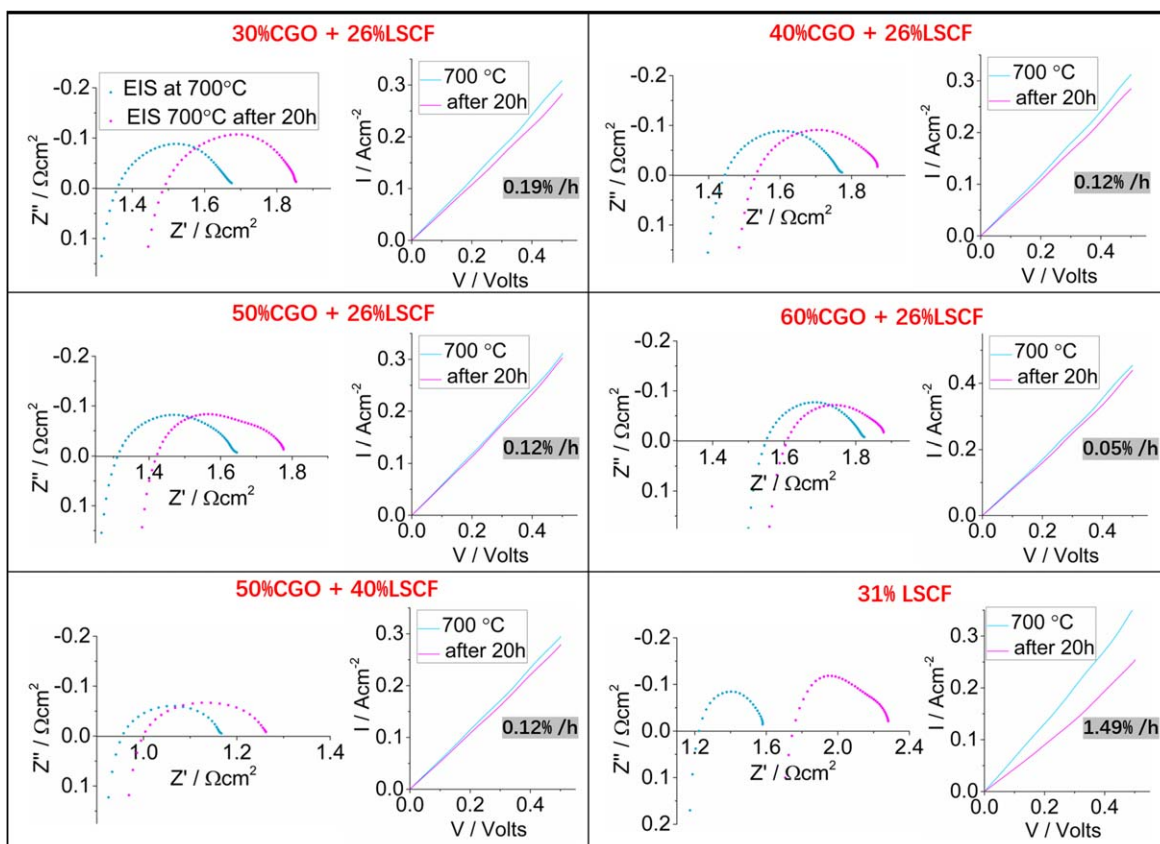


**Figure 2.** EIS and I-V characteristics before and after a 20 h stability test at 0.5 V at 700  $^{\circ}\text{C}$  for the planar cells with various CGO and LSCF volume concentrations. (The rig resistance of 0.2  $\Omega$  is also included).

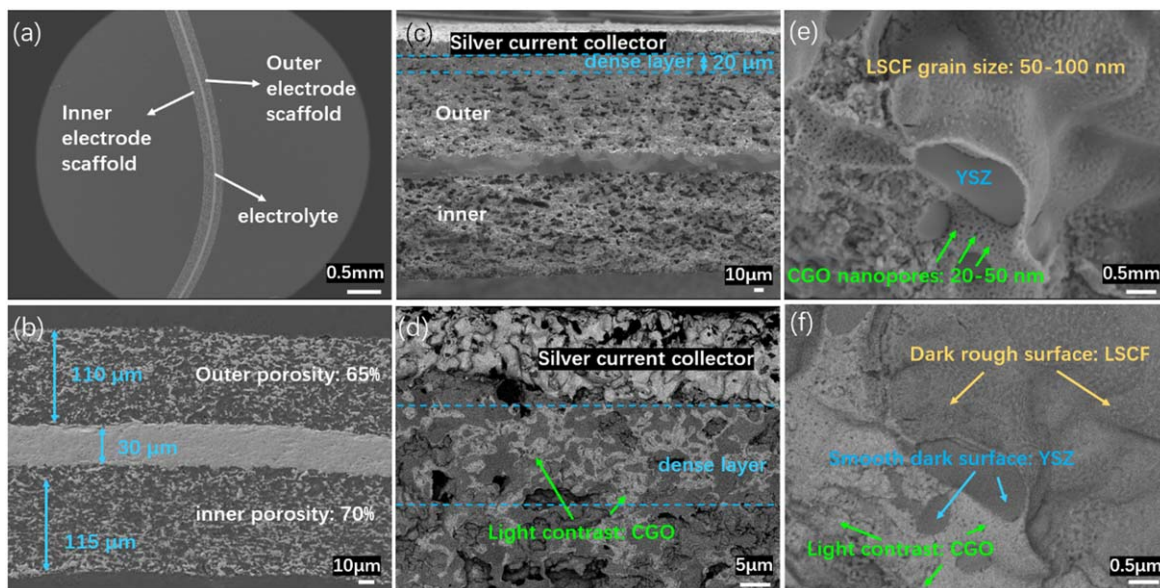


**Figure 3.** SEM images of (a) the cross-section of the as-sintered tubular cell, (c) 50% CGO and 35% LSCF impregnated cell, and (e) the high magnified electrode after impregnation, BSE images of (b) the cross-section of the as-sintered tubular cell immersed with resin, (d) the magnified dense layer in (c), and (f) the corresponding area in (e).

The cross-section microstructure of the tubular cell in Fig. 3a shows that the co-sintered three layers of tape attach well without delamination. The dense YSZ electrolyte is approximately 30  $\mu\text{m}$  thick, and the electrode scaffold is slightly asymmetric, around 110  $\mu\text{m}$  thick outside and 115  $\mu\text{m}$  inside, seen from Fig. 3b. Also, minor differences in porosity are observed between electrodes, 65% for the outer electrode and 70% for the inner electrode. The surface morphologies of both electrodes in Fig. S3 a1 and a2 show that the inner electrode has a smaller grain size range of 0.7–3  $\mu\text{m}$  and the outer electrode 1–5  $\mu\text{m}$ . Also, although it is difficult to measure the pore size due to their irregular shape, one still can recognise the larger pores on the inner electrode surface than the outer electrode. Differences in porosity, pore size and the grain size of electrodes come from the variations in stress distribution of the tubular geometry during co-sintering, further influencing the different sintering behaviour of the outer and inner electrodes. After impregnation, a dense layer of  $\sim 20$   $\mu\text{m}$  is observed on the surface of the outer electrode but not on the inner electrode, seen from Fig. 3c. Further analysis of the BSE image (Fig. 3d) and the EDS maps in Fig. S4 identifies the CGO agglomeration in the dense layer.

The microstructures in Fig. S3 indicate that both surface and bulk porosity decreased after impregnation with 50% CGO, with the outer electrode showing a much lower surface porosity (6%) than the inner layer (23%). Also, the cross-section images in Figs. S3c1 and c2 indicate a concentration gradient of CGO in the outer electrode, with a higher concentration closer to the surface. The lower porosity and smaller pore size (at least on the surface) of the outer electrode could explain the inhomogeneous CGO distribution. The concave geometry could also affect the capillarity forces for driving the solution into the porous layer or the drying process for the infiltration solution migrating to the concave surface,<sup>39</sup> which results in the material's agglomeration on the outer electrode surface. The geometry effect can be verified by the absence of a dense surface layer on the planar cell impregnated with 50% CGO and 40% LSCF shown in Fig. S1. The agglomerated CGO could block the flow of the LSCF solution during its impregnation, resulting in a dense surface layer on the outer electrode.

When the phases are distinguished from the BSE image in Fig. 3f, the SEM image in Fig. 3e shows the well coated YSZ scaffold with the impregnated materials. The CGO phase is porous with many nanopores between 20–50 nm, and the LSCF forms a continuous thin layer with a grain size of 50–100 nm. The BSE

images in Fig. S5 suggest that the LSCF almost entirely covers the CGO layer since the uniform and highly exposed light contrast phase (which is supposed to be CGO) is almost invisible after LSCF impregnation.

The variation of current (oxygen production) with voltage in operating the single oxygen pump tubular cell in the temperature range of 650  $^{\circ}\text{C}$  to 800  $^{\circ}\text{C}$  is presented in Fig. 5a. As can be seen, 1.3 A current is produced at 700  $^{\circ}\text{C}$  with an applied voltage of 0.5 V. However, the current is much lower than expected, basing on the obtained current density of the planar cell, which should be at least 2.5 A for a cell with an electrode area of 3.5  $\text{cm}^2$  and a thinner electrolyte.

The lower performance per surface area in the tubular cell could result from several factors. On the one hand, not all the electrode area is able to be active for the electrochemical reaction. Current density of the tubular cell with a 1.5  $\text{cm}^2$  (cell length of 1.5 cm)-electrode area is much higher than in the cell with a 3.5  $\text{cm}^2$  (cell length of 3 cm)-electrode in the temperature range of 650  $^{\circ}\text{C}$ –750  $^{\circ}\text{C}$ , seen from Fig. S6. The smaller current density in the larger cell may come from the larger temperature variation along the tubular cell as only about 1.5 cm in the vertical distance of the furnace reaches the set 700  $^{\circ}\text{C}$  (Fig. S7). On the other hand, the uneven gas distribution can also give rise to an effective electrode area smaller than 3.5  $\text{cm}^2$ .<sup>47</sup> Moreover, the observed dense layer on the outer electrode in Fig. 3b could block the gas diffusion pathway, and the surface agglomerated CGO would influence the current collection. Last but not least, the poor percolation of LSCF in the outer electrode and its insufficient concentration (35%) could lead to lower electronic conductivity and higher polarisation resistance.

The thermal cycling capability of the single oxygen pump cell was evaluated under potentiostatic mode at 0.5 V, cycled between rapid heating up to 700  $^{\circ}\text{C}$  and cooling down to 100  $^{\circ}\text{C}$ . The result in Fig. 4b demonstrates the rapid response of the current to temperature changes, and there is no current loss after 18 cycles.

The interface between the YSZ scaffold, CGO and LSCF layer after testing at 0.5 V for 15 h was investigated. The EDS maps in Figs. 5a and S8 show that both CGO and LSCF are well coated on the YSZ scaffold. The LSCF phase exists on the outermost layer with a thickness of  $\sim 70$  nm, followed by a thin CGO layer, approximately 30 nm thick (Fig. 5b). Unfortunately, driven by the strain/stress and charge effect, Sr segregation from the LSCF phase toward YSZ is still observed under the application of thin CGO

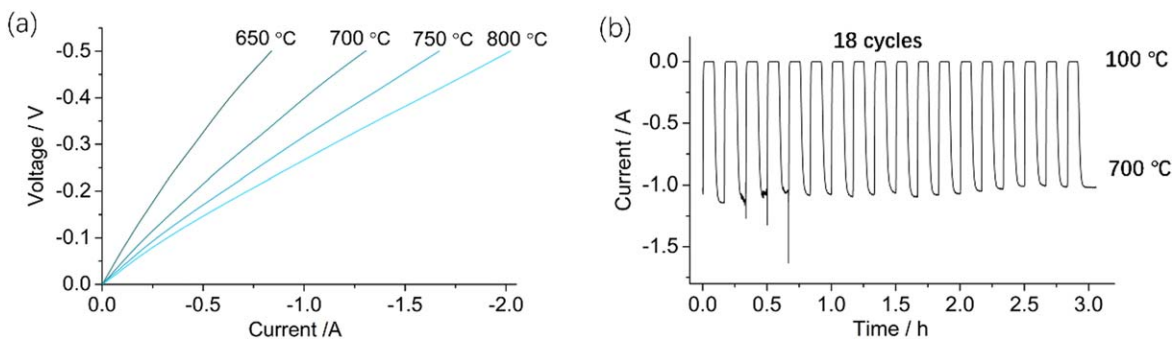


**Figure 4.** (a) IV performance of the single tubular cell (infiltrated with 50% CGO and 35% LSCF) at the temperature range of 650 °C–800 °C, (b) thermal cycling performance between 100 and 700 °C at a constant voltage of 0.5 V.

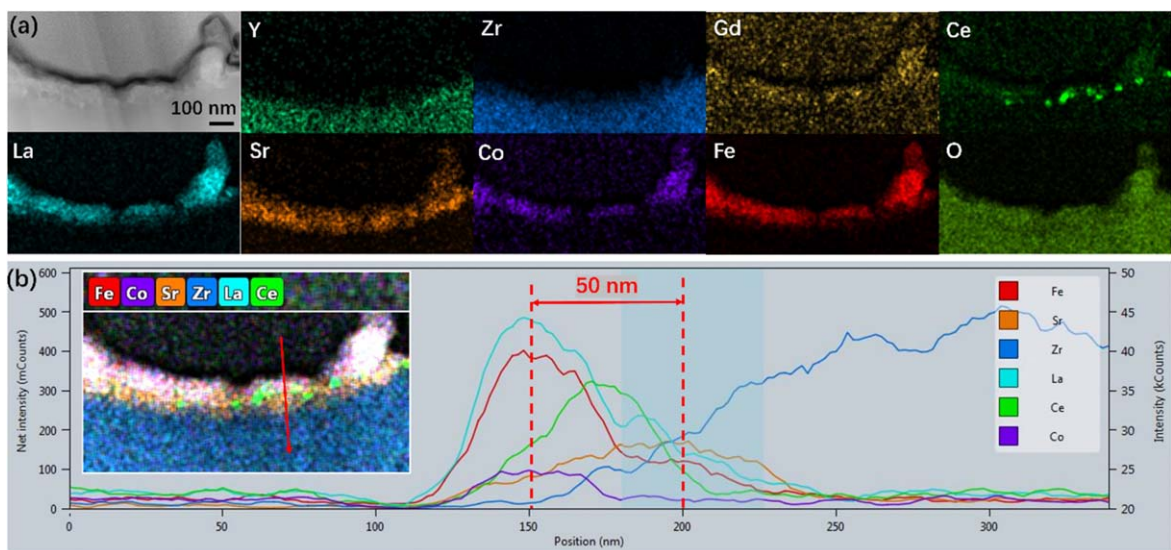


**Figure 5.** (a) TEM image and the corresponding EDS maps of the cross-section of the tubular outer electrode (cathode) after testing at 0.5 V for 15 h at 700 °C, (b) EDS line scanning along the red arrow in the inset EDS map. The tubular cell is infiltrated with 50% CGO and 35% LSCF.

layer, suggested from the maximum intensity of Sr peak locating below the CGO layer.<sup>48</sup> Comparing the peak position of La and Sr, Sr migrates by about 50 nm and is overlapped with YSZ by 20–30 nm. An insulating layer of SrZrO<sub>3</sub> is probably formed in the overlapped area, which can block the ion migration path and lead to cell performance degradation.<sup>24,33,43,49,50</sup>

**Co-cast of the tubular cell with modified impregnation amount.**—Electrochemical performance of the tubular cell was then improved by decreasing the electrolyte thickness and applying co-casting of three layers (YSZ scaffold + YSZ electrolyte + YSZ scaffold). As described above, the tubular cell has shown lower current density than the planar variant due to the insufficient LSCF amount and a dense surface layer of CGO on the outer electrode; here, the CGO and LSCF percentage is optimised to 30% and 45%, respectively.

The new fabricated cell has an electrolyte thickness of only 16 μm, and the symmetric YSZ scaffold of 75–77 μm, shown in Fig. 6a. The electrode scaffold is well bound with the electrolyte without delamination. YSZ electrolyte is fully dense with a few isolated nano-holes (Fig. 6b), and its thickness is compromised by only two-grains size, which will give a small electrolyte resistance from the grain boundary.

As shown in Figs. S9a and S9b, after impregnation with 30% CGO and 45% LSCF, the near-surface area of the outer electrode still looks denser, but it indeed improved compared to the previous tubular cell, with less extent of CGO agglomeration and better LSCF percolation revealed in Figs. S9c–S9f.

The combined effect of higher LSCF concentration, a thinner electrolyte and fully co-cast assembly gave an excellent performance. As seen in Fig. 7a, the R<sub>s</sub> and R<sub>p</sub> of the cell at OCV at 700 °C are 0.17 Ω (including the resistance from the silver wire and stainless steel tube) and 0.01 Ω, respectively. Applying potential decreases the R<sub>s</sub> but does not influence much on R<sub>p</sub>. The I–V test at 700 °C in Fig. 7b shows that the current obtained here is much higher than the one in Fig. 4a. Specifically, with an applied voltage of 0.5 V at 700 °C, 2.8 A current is produced here compared with only 1.3 A in the cell with thicker electrolyte (30 μm) and lower LSCF concentration (35%). The specific energy consumption of 1 kWh m<sup>-2</sup> O<sub>2</sub> is attained at the current of 1.18 A (0.34 A cm<sup>-2</sup>) at 700 °C, which is even higher than the value (0.3 A cm<sup>-2</sup>) at 780 °C reported by Spirin. et al.<sup>20</sup> A key consideration in the design of the oxygen pump is endurance. Therefore, a 27 h-stability test was carried at 700 °C at 0.4 V applied DC bias to investigate cell performance during continuous operation. Shown in Fig. 7c, the current only has a minor variation during the measurement, being 2.01 A at the maximum and 1.98 A after 27 h's test.

**Performance of oxygen pump bundle of four cells.**—A developed single tubular cell was scaled up by connecting four cells in series to assemble an oxygen pump bundle and tested at 700 °C.

The impedances under OCV were measured with various numbers of cells in connection. As shown in Fig. 8a, both R<sub>s</sub> and R<sub>p</sub> increase with more cells connected in series, indicating a good circuit connection in the oxygen pump bundle. The voltages as a function of cell number achieved under the galvanostatic mode of

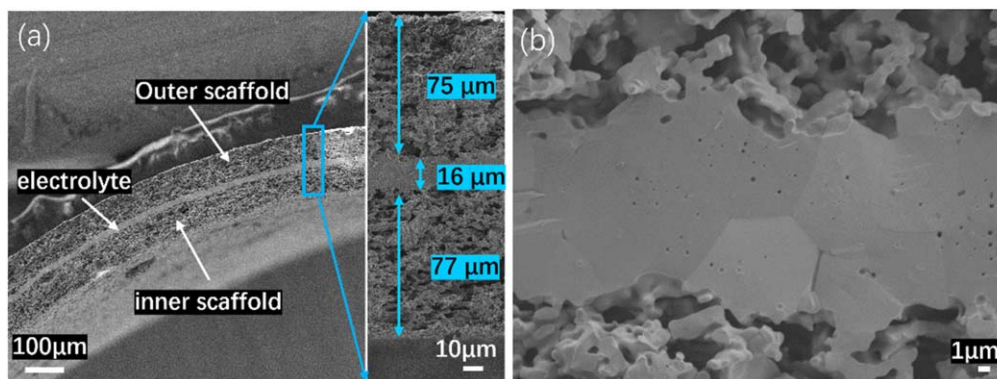


**Figure 6.** SEM images of the cross-section of the (a) tubular cell with an inset of higher magnification, (b) the magnified electrolyte.

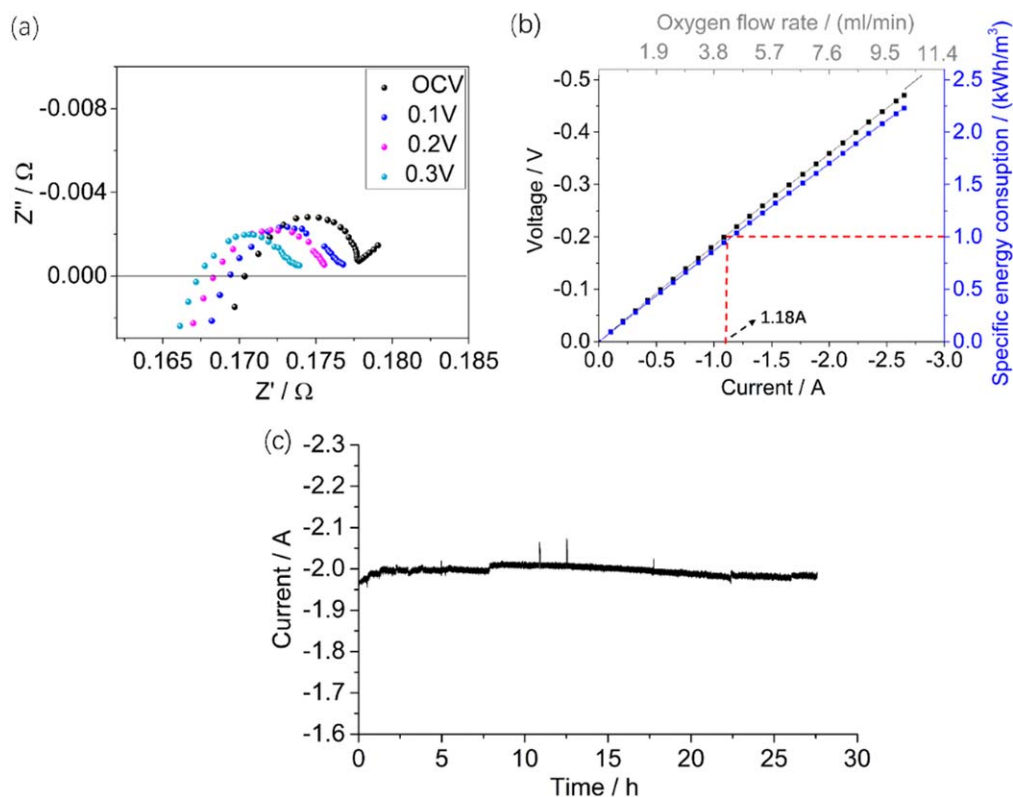


**Figure 7.** Electrochemical measurements of the single tubular cell impregnated with 30% CGO and 45% LSCF at 700 °C. (a) Impedance spectra under OCV and applied potential, (b) IV performance. The missing data point in the potential range above  $-0.45$  V is due to the resolution limit of the Solartron; thus the I–V plot was prolonged to  $-0.5$  V. The oxygen flow rate was calculated according to the corresponding current, and the specific energy consumption was calculated corresponded to the voltage. (c) Stability test under constant voltage of  $0.4$  V.

$0.5$  A are proportionally increased but seem not to be in a linear relationship with the first single-cell (Fig. S10a). This is due to the small variation in the cell property during the cell fabrication process on the one hand, and on the other hand, it is because the resistances from silver wire, stainless steel tube, and instrument are not proportionally enlarged when connecting more cells in series (Fig. S10b). When  $2$  A was applied to the circuit, the outlet gas flow rate ( $Q_{\text{out}}$ ) was shown to be proportional to the cells number in Fig. 8b, further demonstrating the efficient performance of each cell. However, a higher experimentally generated  $Q_{\text{out}}$  was obtained than the theoretical value that calculated according to the Faraday's law, which may come from the leaking at the cell's joining, making air from the cathode leak to the anode side. This can also be verified from the  $\text{N}_2$  signal in the outlet gas MS spectrum in Fig. S11, and the  $\text{O}_2$  purity was calculated to be  $\sim 70\%$ . The leakage is likely to be minor as the bubble in the flask used for measuring  $Q_{\text{out}}$  stopped

moving once the current was withdrawn. One should also notice that the generated  $\text{O}_2$  on the anode side can also leak from the cathode, resulting in the lower purity in the outlet. Another possible reason could be the discrepant condition between the experiment and calculation,<sup>20</sup> e.g., the calculation is based on assuming gas to be  $25$  °C. By varying the applied current, a linear relationship is observed between the current (in the range of  $0.25$ – $2$  A) and voltage in the bundle, with approximately  $1.09$  V required to pass  $2$  A in the bundle (Fig. 8c). The experimental  $Q_{\text{out}}$  increases correspondingly with current, obtaining a flow rate of  $35.4$   $\text{ml min}^{-1}$  at  $2$  A. The relationship between the measured  $Q_{\text{out}}$  and the consumed power is plotted in Fig. 8d. Again, the leakage and the inconsistent condition leads to the measured value above the calculated one. While  $2.18$  W electric energy would generate a theoretical amount of  $30.4$   $\text{ml min}^{-1}$  ( $1.821$   $\text{h}^{-1}$ )  $\text{O}_2$  in the oxygen pump bundle,  $35.4$   $\text{ml min}^{-1}$  ( $2.12$   $\text{h}^{-1}$ ) of the outlet gas was measured in this system.

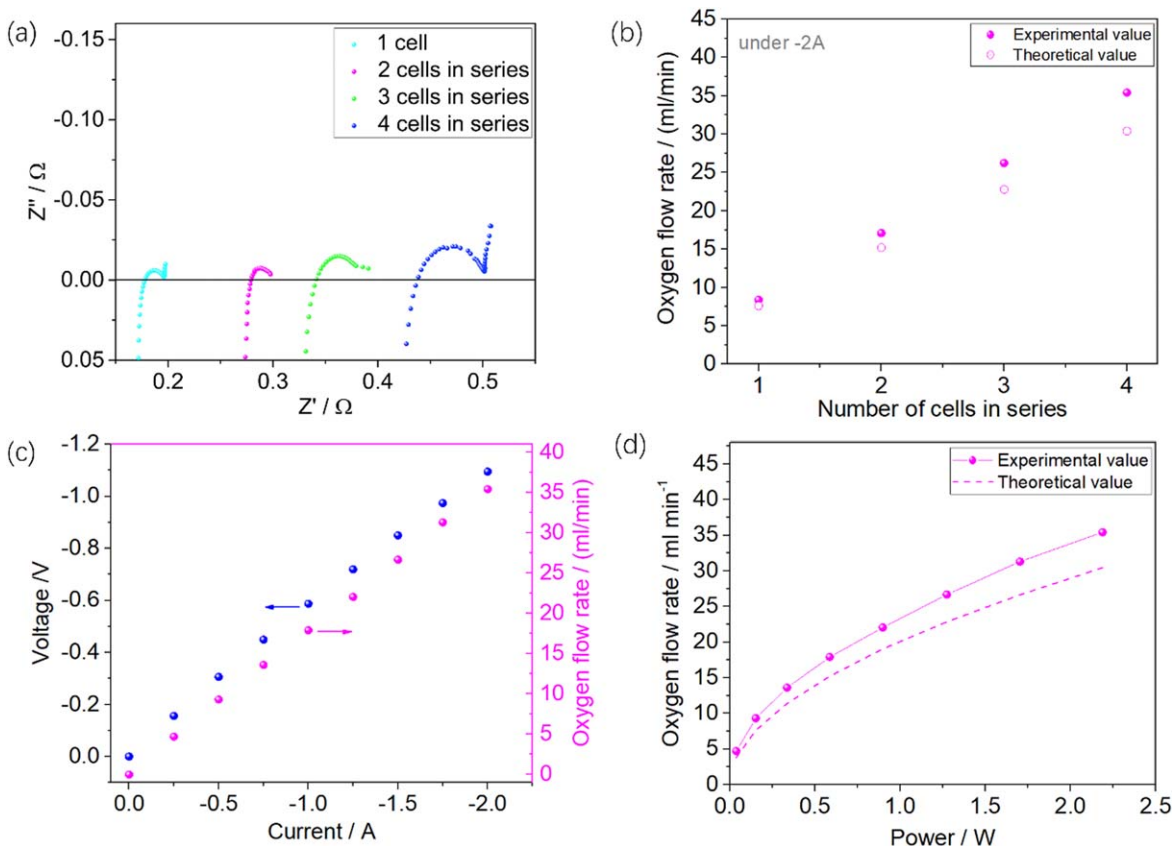


**Figure 8.** Electrochemical test of the four-cells oxygen pump bundle at 700 °C. (a) EIS at OCV measured with involving different numbers of cells, (b) the measured oxygen flow rate under 2 A as a function of cells number in series, (c) the I–V performance and the experimentally measured oxygen flow rate, and (d) the variation of the oxygen flow rate of the four-cells bundle with power consumption ( current from 0.25 A to 2 A).

The stability of the oxygen pump bundle was evaluated by both current cycle and thermal cycle stability. For each current cycle, the oxygen pump bundle ran at 2 A for 2 h, and the current was withdrawn for 1 h in the interval. As shown in Fig. 9a, there is vibration in the voltage during the first cycle, but it recovers to the starting value after 1.5 h. The vibration may be due to the activation process of the electrode materials under current by promoting the formation of electrode/electrolyte interface or re-organising the nanopores formation.<sup>51,52</sup> The voltage remains stable from the 2nd to the 5th current cycle and even gets smaller than in the 1st cycle. For the thermal stability test, rapid heating up and cooling down was applied (20 °C min<sup>-1</sup>). The power consumption for the oxygen

pump bundle running at 2 A and the experimental oxygen flow rate were measured after heating up to 700 °C, shown in Fig. 9b. After five thermal cycles, the power required for maintaining the theoretical oxygen flow at the constant level of 1.82 l hr<sup>-1</sup> (2 A current) increased by 12%. The measured gas flow rate (~2.12 l h<sup>-1</sup>) remains stable with only slight vibration, indicating that the cells are robust and no serious cracks occur during the thermal cycle.

## Conclusions

A highly performing electrochemical oxygen pump was fabricated based on solid oxide tubular cells, manufactured by tape co-casting techniques (YSZ skeleton) and impregnation of functional

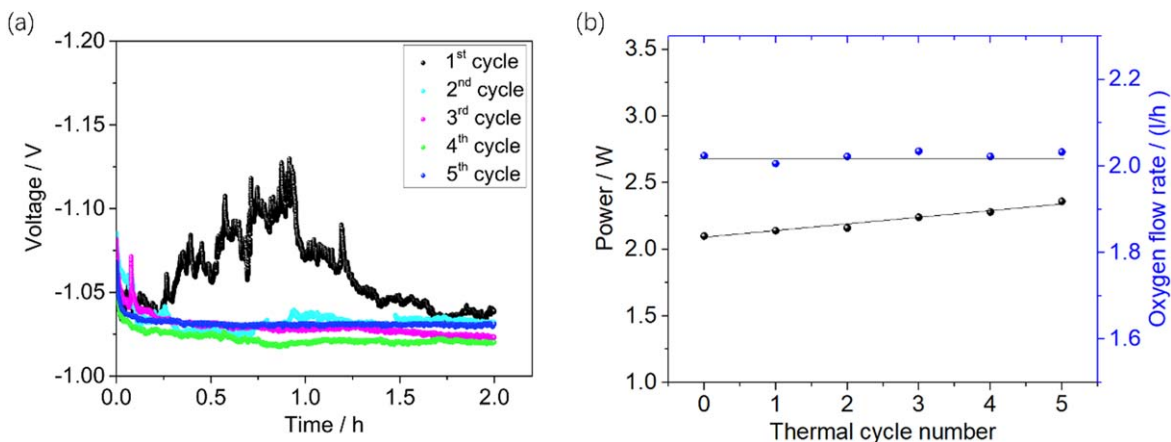


**Figure 9.** The oxygen pump bundle stability test at 700 °C. (a) Current cycle test. In each cycle, 2 A passed through the cell bundle for 2 h and was withdrawn for 1 h in the interval. (b) Thermal cycle test.



electrode materials (CGO and LSCF). The cell has a very thin YSZ electrolyte ( $\sim 16 \mu\text{m}$ ) and symmetrical YSZ porous electrodes scaffold ( $\sim 75 \mu\text{m}$ ). The CGO barrier layer on the scaffold is approximately 80 nm thick, and LSCF is about 100 nm in thickness. Whilst the optimized impregnation content is 50% CGO and 40% LSCF on the planar cell, it need to be modified to 30% CGO and 45% LSCF when working on the tubular cell, due to the geometry introduced dense surface layer (mainly comes from the agglomerated CGO) on the outer electrode.

The optimised single tubular cell shows an excellent performance, producing 2.8 A under 0.5 V voltage at only 700 °C. The specific energy consumption of  $1 \text{ kWh m}^{-2} \text{ O}_2$  reaches at the current of 1.18 A ( $0.34 \text{ A cm}^{-2}$ ) at 700 °C. Unfortunately, the CGO layer is unable to prevent the Sr segregation from LSCF towards YSZ, and 50 nm- migration of Sr was observed after testing the cell at 0.5 V for 15 h. When scaled up, the oxygen pump bundle compromised by four cells consumes 2.18 W of electric power at 700 °C to produce theoretical  $1.82 \text{ l hr}^{-1} \text{ O}_2$ . The oxygen pump bundle is robust during the current and thermal cycling test. However, the measured  $\text{O}_2$  flow rate is higher than the calculated value, which may be due to the leaking at the joining part of the cell and the inconsistent condition between the test and calculation. Further modification on the sealing of these cells prepared via tape co-casting need to be worked on to obtain a higher purity of  $\text{O}_2$ .

### Acknowledgments

The authors would like to thank Dr. Aron Naden for working on the FIB sampe preparation and TEM characterisation. Also, the authors would like to acknowledge the Scottish Funding Council for support this work and EPSRC for the Scios and EM equipment (EP/L017008/1, EP/T019298/1).

### ORCID

John Thomas Sirr Irvine  <https://orcid.org/0000-0002-8394-3359>

### References

- H. Häring, "The air gases nitrogen, oxygen and argon." *Industrial Gases Processing*, 9 (2008).
- R. J. Allam, "Improved oxygen production technologies." *Energy Procedia*, 1, 461 (2009).
- A. Ebrahimi, M. Meratizaman, H. A. Reyhani, O. Pourali, and M. Amidpour, "Energetic, exergetic and economic assessment of oxygen production from two columns cryogenic air separation unit." *Energy*, 90, 1298 (2015).
- T. Burdyny and H. Struchtrup, "Hybrid membrane/cryogenic separation of oxygen from air for use in the oxy-fuel process." *Energy*, 35, 1884 (2010).
- B. Adhikari, C. J. Orme, J. R. Klaehn, and F. F. Stewart, "Technoeconomic analysis of oxygen-nitrogen separation for oxygen enrichment using membranes." *Sep. Purif. Technol.*, 268, 118703 (2021).
- J. Santos, P. Cruz, T. Regala, F. Magalhaes, and A. Mendes, "High-purity oxygen production by pressure swing adsorption." *Ind. Eng. Chem. Res.*, 46, 591 (2007).
- S. Farooq, D. Ruthven, and H. Boniface, "Numerical simulation of a pressure swing adsorption oxygen unit." *Chem. Eng. Sci.*, 44, 2809 (1989).
- E. Akulinin, O. Golubyatnikov, D. Dvoretzky, and S. Dvoretzky, "Optimization and analysis of pressure swing adsorption process for oxygen production from air under uncertainty." *Chemical Industry and Chemical Engineering Quarterly*, 26, 89 (2020).
- N. Miura, H. Ikeda, and A. Tsuchida, " $\text{Sr}_{1-x}\text{Ca}_x\text{FeO}_{3-\delta}$  as a new oxygen sorbent for the high-temperature pressure-swing adsorption process." *Ind. Eng. Chem. Res.*, 55, 3091 (2016).
- J. Phair and S. Badwal, "Materials for separation membranes in hydrogen and oxygen production and future power generation." *Sci. Technol. Adv. Mater.*, 7, 792 (2006).
- A. Klimashin and V. Belousov, "Oxygen ion transport in molten oxide membranes for air separation and energy conversion." *J. Electrochem. Soc.*, 164, H5353 (2017).
- V. Khariton, A. Yaremchenko, A. Kovalevsky, A. Viskup, E. Naumovich, and P. Kerko, "Perovskite-type oxides for high-temperature oxygen separation membranes." *J. Membr. Sci.*, 163, 307 (1999).
- S. Aasland, I. Tangen, K. Wiik, and R. Ødegård, "Oxygen permeation of  $\text{SrFe}_{0.67}\text{Co}_{0.33}\text{O}_{3-\delta}$ ." *Solid State Ionics*, 135, 713 (2000).
- T. Ishihara, T. Yamada, H. Arikawa, H. Nishiguchi, and Y. Takita, "Mixed electronic-oxide ionic conductivity and oxygen permeating property of Fe-, Co- or Ni-doped  $\text{LaGaO}_3$  perovskite oxide." *Solid State Ionics*, 135, 631 (2000).
- S. Kim, Y. Yang, R. Christoffersen, and A. Jacobson, "Determination of oxygen permeation kinetics in a ceramic membrane based on the composition  $\text{SrFeCo}_{0.5}\text{O}_{3.25-\delta}$ ." *Solid State Ionics*, 109, 187 (1998).
- V. V. Belousov, S. V. Fedorov, and M. S. Sedov, "Innovative MIEC-redox oxygen separation membranes with combined diffusion-bubbling mass transfer: a brief review." *J. Electrochem. Soc.*, 166, H573 (2019).
- D. L. Meixner, D. D. Bregel, B. T. Henderson, J. M. Abrardo, M. A. Wilson, D. M. Taylor, and R. A. Cutler, "Electrochemical oxygen separation using solid electrolyte ion transport membranes." *J. Electrochem. Soc.*, 149, D132 (2002).
- K. Sridhar and B. Vaniman, "Oxygen production on Mars using solid oxide electrolysis." *Solid State Ionics*, 93, 321 (1997).
- J. Guan, R. Doshi, G. Lear, K. Montgomery, E. Ong, and N. Minh, "Ceramic oxygen generators with thin-film zirconia electrolytes." *J. Am. Ceram. Soc.*, 85, 2651 (2002).
- A. V. Spirin, A. V. Nikonov, A. S. Lipilin, S. N. Parandin, V. V. Ivanov, V. R. Khrustov, A. V. Valentev, and V. I. Krutikov, "Electrochemical cell with solid oxide electrolyte and oxygen pump thereof." *Russ. J. Electrochem.*, 47, 569 (2011).
- V. Subotić, S. Futamura, G. F. Harrington, J. Matsuda, K. Natsukoshi, and K. Sasaki, "Towards understanding of oxygen electrode processes during solid oxide electrolysis operation to improve simultaneous fuel and oxygen generation." *J. Power Sources*, 492, 229600 (2021).
- N. Hedayat, Y. Du, and H. Ilkhani, "Review on fabrication techniques for porous electrodes of solid oxide fuel cells by sacrificial template methods." *Renew. Sustain. Energy Rev.*, 77, 1221 (2017).
- N. Sammes, Y. Du, and R. Bove, "Design and fabrication of a 100 W anode supported micro-tubular SOFC stack." *J. Power Sources*, 145, 428 (2005).
- S.-Y. Park, J. H. Ahn, C.-W. Jeong, C. W. Na, R.-H. Song, and J.-H. Lee, "Ni-YSZ-supported tubular solid oxide fuel cells with GDC interlayer between YSZ electrolyte and LSCF cathode." *Int. J. Hydrogen Energy*, 39, 12894 (2014).
- D. Chen, Y. Xu, B. Hu, C. Yan, and L. Lu, "Investigation of proper external air flow path for tubular fuel cell stacks with an anode support feature." *Energy Convers. Manage.*, 171, 807 (2018).
- W. Bujalski, C. M. Dikwal, and K. Kendall, "Cycling of three solid oxide fuel cell types." *J. Power Sources*, 171, 96 (2007).
- Z. Liu, M.-F. Han, and W.-T. Miao, "Preparation and characterization of graded cathode  $\text{La}_{0.6}\text{Sr}_{0.4}\text{Co}_{0.2}\text{Fe}_{0.8}\text{O}_{3-\delta}$ ." *J. Power Sources*, 173 (2007).
- H. A. Rahman, A. Muchtar, N. Muhamad, and H. Abdullah, "Structure and thermal properties of  $\text{La}_{0.6}\text{Sr}_{0.4}\text{Co}_{0.2}\text{Fe}_{0.8}\text{O}_{3-\delta}$ -SDC carbonate composite cathodes for intermediate-to low-temperature solid oxide fuel cells." *Ceram. Int.*, 38, 1571 (2012).
- B. Zhu, "Advantages of intermediate temperature solid oxide fuel cells for traction applications." *J. Power Sources*, 93, 82 (2001).
- C. Lei, M. F. Simpson, and A. V. Virkar, "Investigation of electrode kinetics of porous La-Sr-Co-Fe-oxide (LSCF) electrodes on yttria-stabilized zirconia (YSZ) electrolyte using alternating current (AC) and direct current (DC) methods." *J. Electrochem. Soc.*, 168, 064510 (2021).
- H. Fan, M. Keane, N. Li, D. Tang, P. Singh, and M. Han, "Electrochemical stability of  $\text{La}_{0.6}\text{Sr}_{0.4}\text{Co}_{0.2}\text{Fe}_{0.8}\text{O}_{3-\delta}$ -infiltrated YSZ oxygen electrode for reversible solid oxide fuel cells." *Int. J. Hydrogen Energy*, 39, 14071 (2014).
- G. C. Kostoglouidis, G. Tsiniarakis, and C. Fitos, "Chemical reactivity of perovskite oxide SOFC cathodes and yttria stabilized zirconia." *Solid State Ionics*, 135, 529 (2000).
- S. P. Jiang, "Development of lanthanum strontium cobalt ferrite perovskite electrodes of solid oxide fuel cells—a review." *Int. J. Hydrogen Energy*, 44, 7448 (2019).
- S. Uhlenbruck, T. Moskalewicz, N. Jordan, H.-J. Penkalla, and H. Buchkremer, "Element interdiffusion at electrolyte-cathode interfaces in ceramic high-temperature fuel cells." *Solid State Ionics*, 180, 418 (2009).
- M. Hubert, J. Laurencin, P. Cloetens, J. Mouglin, D. F. Sanchez, S. Pylypko, M. Morales, A. Morata, B. Morel, and D. Montinaro, "Solid oxide cell degradation operated in fuel cell and electrolysis modes: a comparative study on Ni Agglomeration and LSCF destabilization." *ECS Trans.*, 78, 3167 (2017).
- E. Effori, J. Laurencin, E. D. R. Silva, M. Hubert, T. David, M. Petitjean, G. Geneste, L. Dessemond, and E. Siebert, "An elementary kinetic model for the LSCF and LSCF-CGO electrodes of solid oxide cells: impact of operating conditions and degradation on the electrode response." *J. Electrochem. Soc.*, 168, 044520 (2021).
- D. The, S. Grieshammer, M. Schroeder, M. Martin, M. Al Daroukh, F. Tietz, J. Schefeld, and A. Brisse, "Microstructural comparison of solid oxide electrolyser cells operated for 6100 h and 9000 h." *J. Power Sources*, 275, 901 (2015).
- S. P. Jiang, "Nanoscale and nano-structured electrodes of solid oxide fuel cells by infiltration: advances and challenges." *Int. J. Hydrogen Energy*, 37, 449 (2012).
- J. M. Vohs and R. J. Gorte, "High-performance SOFC cathodes prepared by infiltration." *Adv. Mater.*, 21, 943 (2009).
- Y. Cheng, T.-S. Oh, R. Wilson, R. J. Gorte, and J. M. Vohs, "An investigation of LSF-YSZ conductive scaffolds for infiltrated SOFC cathodes." *J. Electrochem. Soc.*, 164, F525 (2017).
- K. M. Nowicki, H. Zeng, and J. T. Irvine, "Manufacturing and electrochemical evaluation of SOFCroll with the  $\text{La}_{0.43}\text{Ca}_{0.37}\text{Ni}_{0.06}\text{Ti}_{0.94}\text{O}_{3-\gamma}\text{Zr}_{0.92}\text{Y}_{0.08}\text{O}_{2-\gamma}$  anode." *ECS Trans.*, 91, 139 (2019).
- J. M. Vohs and R. J. Gorte, "High-performance SOFC cathodes prepared by infiltration." *Adv. Mater.*, 21, 943 (2009).
- N. Ai, S. He, N. Li, Q. Zhang, W. D. A. Rickard, K. Chen, T. Zhang, and S. P. Jiang, "Suppressed Sr segregation and performance of directly assembled  $\text{La}_{0.6}\text{Sr}_{0.4}\text{Co}_{0.2}\text{Fe}_{0.8}\text{O}_{3-\delta}$  oxygen electrode on  $\text{Y}_2\text{O}_3\text{-ZrO}_2$  electrolyte of solid oxide electrolysis cells." *J. Power Sources*, 384, 125 (2018).
- V. Yurkiv, R. Costa, Z. Ilhan, A. Ansar, and W. G. Bessler, "Impedance of the surface double layer of LSCF/CGO composite cathodes: an elementary kinetic model." *J. Electrochem. Soc.*, 161, F480 (2014).

45. S. Wang, T. Kato, S. Nagata, T. Honda, T. Kaneko, N. Iwashita, and M. Dokiya, "Performance of a  $\text{La}_{0.6}\text{Sr}_{0.4}\text{Co}_{0.8}\text{Fe}_{0.2}\text{O}_3\text{-Ce}_{0.8}\text{Gd}_{0.2}\text{O}_{1.9}\text{-Ag}$  cathode for ceria electrolyte SOFCs.." *Solid State Ionics*, **146**, 203 (2002).
46. Y. Zhang, M. Han, and Z. Sun, "High performance and stability of nanocomposite oxygen electrode for solid oxide cells." *Int. J. Hydrogen Energy*, **45**, 5554 (2020).
47. D. Cui, Y. Ji, C. Chang, Z. Wang, and X. Xiao, "Influence of fuel flow rate on the performance of micro tubular solid oxide fuel cell." *Int. J. Hydrogen Energy*, **45**, 13459 (2020).
48. N. Ai, S. He, N. Li, Q. Zhang, W. D. Rickard, K. Chen, and T. Zhang, "Suppressed Sr segregation and performance of directly assembled  $\text{La}_{0.6}\text{Sr}_{0.4}\text{Co}_{0.2}\text{Fe}_{0.8}\text{O}_{3-\delta}$  oxygen electrode on  $\text{Y}_2\text{O}_3\text{-ZrO}_2$  electrolyte of solid oxide electrolysis cells." *J. Power Sources*, **384**, 125 (2018).
49. Z. He, L. Zhang, S. He, N. Ai, K. Chen, Y. Shao, and S. P. Jiang, "Cyclic polarization enhances the operating stability of  $\text{La}_{0.57}\text{Sr}_{0.38}\text{Co}_{0.18}\text{Fe}_{0.72}\text{Nb}_{0.1}\text{O}_{3-\delta}$  oxygen electrode of reversible solid oxide cells." *J. Power Sources*, **404**, 73 (2018).
50. J. Laurencin, M. Hubert, D. F. Sanchez, S. Pylypko, M. Morales, A. Morata, B. Morel, D. Montinaro, F. Lefebvre-Joud, and E. Siebert, "Degradation mechanism of  $\text{La}_{0.6}\text{Sr}_{0.4}\text{Co}_{0.2}\text{Fe}_{0.8}\text{O}_{3-\delta}/\text{Gd}_{0.1}\text{Ce}_{0.9}\text{O}_{2-\delta}$  composite electrode operated under solid oxide electrolysis and fuel cell conditions." *Electrochim. Acta*, **241**, 459 (2017).
51. X. Sun, P. Hendriksen, M. Mogensen, and M. Chen, "Degradation in solid oxide electrolysis cells during long term testing." *Fuel Cells*, **19**, 740 (2019).
52. Z. He, L. Zhang, S. He, N. Ai, K. Chen, and Y. Shao, "Cyclic polarization enhances the operating stability of  $\text{La}_{0.57}\text{Sr}_{0.38}\text{Co}_{0.18}\text{Fe}_{0.72}\text{Nb}_{0.1}\text{O}_{3-\delta}$  oxygen electrode of reversible solid oxide cells.." *J. Power Sources*, **404**, 73 (2018).